Phases: from nuclei to quantum dots

D.J. Dean[a*]

[a]Physics Division, Oak Ridge National Laboratory P.O. Box 2008, Oak Ridge, Tennessee 37831 USA

Many confined quantum systems exhibit intrinsic shapes that may be perturbed or qualitatively changed as a function of parameters such as particle number, temperature, angular frequency, and magnetic field. In this proceedings, I explore various manifestations of shapes and their changes in both selected nuclei and semiconductor quantum dots.

1. Introduction

Confined quantum many-body systems of a given particle number exhibit a variety of intrinsic shape characteristics as a function of increasing external field, and internal thermal excitation. The shell model is an important tool for the theoretical description of these various structures and transitions in nuclei. Another system in which correlations beyond the mean field may play an important role is semiconductor quantum dots. In this proceedings, I will compare nuclei and quantum dots and their various deformation properties. I will report on shell-model calculations in nuclei and some very recent mean-field calculations in quantum dots. I will also discuss a first application of auxiliary field Monte Carlo (AFMC) techniques to the quantum dot problem.

2. Phases in nuclei

Nuclei often exhibit different intrinsic structures within the same system. Experimental and theoretical comparisons for ^{56}Ni confirmed the existence of a spherical ground-state band and a prolate deformed band beginning with a measured 2^+ state at 5.3 MeV excitation energy [1] (the second 0^+ state was experimentally inaccessible). This structure, which is present in shell-model calculations, was shown to have an intrinsic deformation by investigating the energy surface generated from cranked Hartree-Fock calculations [2]. This is just one example demonstrating how nuclear spectra often exhibit a band structure that is related to the intrinsic deformation in the system.

Some nuclei show interesting structure in their ground states. For example, nuclei in the ^{124}Xe region are known to be γ-soft. Detailed shell-model Monte Carlo (SMMC) calculations in this region confirmed that effective two-body interactions will give rise to such structures [3]. As one increases the temperature in these systems, they tend toward

*This research was sponsored by the U.S. Department of Energy under Contract No. DE-AC05-00OR22725 managed by UT-Battelle, LLC.

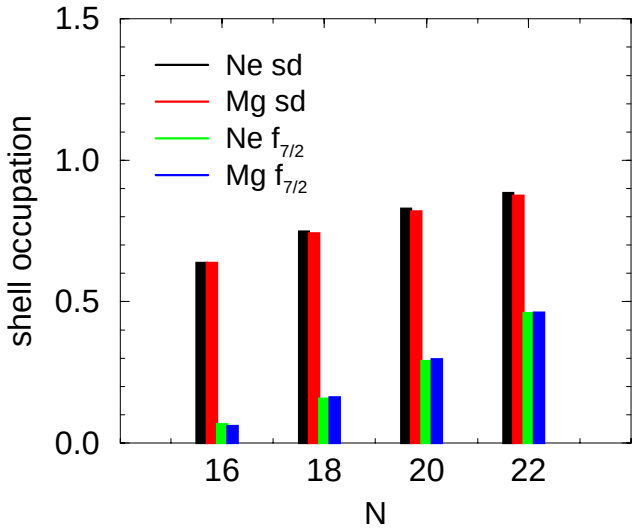

Figure 1. Occupations of the *sd*-*fp* shell for the Ne and Mg chains near $N = 20$.

sphericity. This effect has also been seen in rare-earth calculations [4,5]. Many rare-earth systems are known to have well-deformed ground states. SMMC calculations of intrinsic shapes in these nuclei confirm this in the shell-model context by using a Kumar-Baranger effective interaction [5].

Another interesting phenomena occurs when one approaches shell closures in neutron-rich nuclei. For example, many calculations suggest that in ^{32}Mg the $0f_{7/2}$ sub-shell begins to fill before the *sd*-shell is completely full. The large $B(E2)$ value of ^{32}Mg [6] cannot be explained unless one allows neutrons to occupy *fp*-shell orbitals. Recent SMMC results [7,8] confirm the picture that an island of inversion exists in the ^{32}Mg region [9]. These calculations were performed using the SMMC technique in the full $1s$-$0d$-$0f$-$1p$ model space. The effective shell-model interaction was derived from the realistic charge-dependent Bonn potential [10], with modifications to the monopole terms [11] to alleviate difficulties in the saturation properties of the interaction. Since this calculation was performed in two major oscillator shells, extrapolation procedures to eliminate center-of-mass contamination of the energies were implemented for SMMC technique. With the center-of-mass elimination and a realistic effective interaction, we were able to reproduce both ground-state masses and $B(E2)$ values across the *sd*-*fp* region, both for stable and unstable nuclei. Details are given in [7]. The occupations are shown in Fig. 1 for a chain of Mg and Ne nuclei near $N = 20$. Approximately two neutrons occupy the *fp* shell at $N = 20$, while at $N = 24$ the *sd*-shell is nearly full.

Recently, Barmore et al. [12] investigated the deformation properties of the *sd*-*fp* shell-model interaction used in the SMMC calculations just described. By constraining the deformation in the HFB Hamiltonian, the energy surface may be calculated as a function of deformation. Preliminary results are shown in Fig. 2 for the ^{32}Mg region using two interactions, HJZ from Ref. [7] and WBM, a modified version of the Warburton-Brown interaction [13]. Clearly, this region exhibits a large amount of shape coexistence, which is another feature of interacting fermion systems.

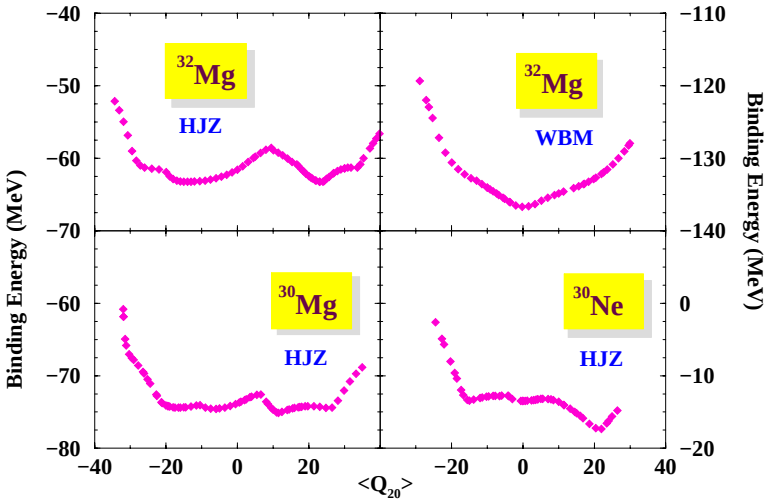

Figure 2. Constrained HFB energies for ^{32}Mg. I compare the interaction HJZ from Ref. [7] and WBM, a slightly modified version of the Warburton-Brown interaction [13] for the same region.

3. Phases in quantum dots

I now turn to another confined quantum mechanical system that exhibits interesting many-body features. Semi-conductor quantum dots are typically formed in III-V substrates, such as GaAs. They may be laterally constructed so that their spatial dimension in the vertical dimension (z direction) is small compared to the horizontal (x, y) dimensions. The GaAs may be constructed in such a way that a physical confining barrier is also included, thus giving rise to confinement in all three dimensions. Electrons may then be placed into this confined structure by conductance spectroscopy, and the system may be studied. The correlations among the electrons are fairly strong and have been experimentally shown to require many-body techniques for their description [14]. In the following I will briefly describe some interesting thermal effects within these systems, and I will discuss a first application of AFMC techniques to quantum dots.

3.1. Quantum dots in magnetic fields: thermal response of broken symmetry phases

In studies of many-body phenomena in quantum dots, experimental efforts have focused on mapping the magnetic field dependence of their ground-state structure by measuring the chemical potential via capacitance spectroscopy [15]. Cusps and steps in the chemical potential were found to clearly separate different ranges of magnetic fields [15,14]. These features were identified with phase transitions in the charge density of the quantum dot. At magnetic field strengths on the order of a few tesla, all electrons become spin-polarized initiating the maximum density droplet (MDD) phase [15], in which the density is constant and homogeneous at the maximum value that can be reached in the lowest Landau level. The stability of the MDD is determined by a competition among the kinetic energy, ex-

ternal confinement, the Coulomb repulsion between electrons, and the attraction created by the Coulomb exchange term. For increasing magnetic field, the charge-density distribution of the droplet reconstructs [16] with a ring of electrons breaking off from the MDD phase. This edge reconstruction has been shown via mean-field [17] and density functional theory [18] calculations to result from a rotational symmetry-breaking phase transition from the MDD to a Wigner molecule or Wigner crystal phase. These calculations are in good qualitative agreement with recent experimental results where instabilities of the MDD state and other transitions in the high magnetic field region were accompanied by a redistribution of the charge density [14].

In describing the ground-state and low-lying (intra-band) excitations of the N-electron semiconductor nanostructures, it is often sufficient to restrict consideration to the conduction band using the effective-mass approximation [19]. We consider the problem of N electrons of effective mass m^* in a plane, (x, y), confined by an external parabolic potential, $V(r) = \frac{1}{2}m^*\omega_0^2 r^2$, and subject to a strong magnetic field $\vec{B} = B_0\vec{e}_z$. We consider the Zeeman splitting but neglect the spin-orbit interaction. The Hamiltonian for such a system is

$$\hat{H} = \sum_i \left[\frac{\left(\vec{p} - \frac{e}{c}\vec{A}\right)^2}{2m^*} + V(r_i) + \frac{g^*\mu_B}{\hbar}\vec{B}\cdot\vec{S}_i \right] + \sum_{i<j} \frac{e^2}{\varepsilon|\vec{r}_i - \vec{r}_j|} \,, \tag{1}$$

where the vector potential is $\vec{A}(\vec{r}_i) = (B_0/2)(-y_i, x_i, 0)$, $g^* = 0.54$, $\varepsilon = 12.9$, $m^* = 0.067m_e$, and $\hbar\omega_0 = 3$ meV.

We solve this equation at the finite-temperature Hartree–Fock level [20]. We use a Fock–Darwin basis expansion to solve the finite-temperature Hartree-Fock equations. Since we use a high (≈ 12 T) magnetic field, we consider only angular momentum states with the $n = 0$ principal quantum number. The electrons carry spin, and so our states are labeled by $k = \{l_k, s_k\}$, where l_k is the angular momentum projection of the k-th state and s_k is the spin of that state. We found convergence using fifty states for the $N \leq 8$ systems. We also checked our zero-temperature results with other publications [17] for various numbers of electrons in the dot and found satisfactory agreement.

We begin the discussion of our results by investigating the electron charge, angular momentum, and spin densities as a function of increasing temperature for the $N = 6$ system at $B_0 = 12.15$ T. We show densities at representative temperatures of 3.87 K (the low temperature limit, $\nu = 6$), 11.97 K (before the first phase transition, $\nu = 6$), 13.65 K (in the second phase, $\nu = 5$), and 14.32 K (in the third phase, $\nu = 4$), where ν is the number of definable high-density regions (or vortices) in the charge density plots. The density, shown in Fig. 3a-d, begins as a fairly well-defined Wigner crystal at 3.87 K, which exhibits some degree of thermal broadening at 11.97 K. The $\nu = 5$ and $\nu = 4$ phases continue to show a similar amount of density in the remaining vortices, while the density of the thermally dissipated vortices have effectively spread through the entire dot. The angular momentum along the B-field direction, shown in Fig. 3e-h, exhibits well-defined structures at low temperatures which tend to decrease rapidly as one moves through the various phases. Although the high charge density regions in the $\nu = 4$ phase are still well defined, the angular momentum in this high-temperature phase has nearly washed out. Finally, we show in Fig. 3i-l the spin density defined as $\rho_s(x, y) =$

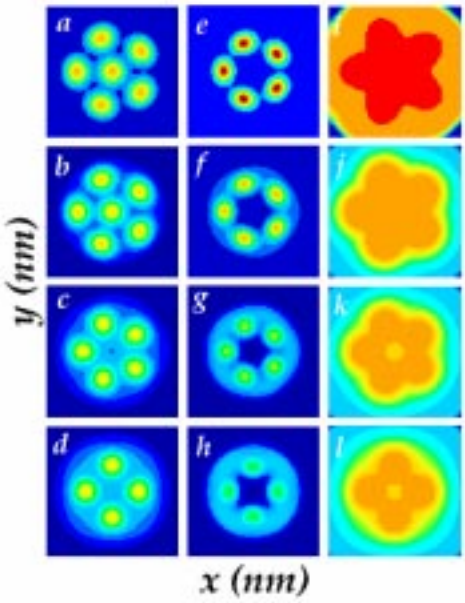

Figure 3. Panels a-d, the charge density; panels e-h, the angular momentum density (in the z-direction); panels i-l, the spin density. In each panel, -8 nm$\leq x, y \leq 8$ nm.

$[\rho_\uparrow(x,y) - \rho_\downarrow(x,y)] \,/\, [\rho_\uparrow(x,y) + \rho_\downarrow(x,y)]$, where $\rho_\uparrow$ ($\rho_\downarrow$) refer to the spin up (down) density. At these temperatures, little appreciable spin depolarization occurs and the spin density remains above 0.8 for the entire region where there is appreciable charge density.

The suddenness of the phase transitions seen in Fig. 3 become quite evident when the internal energy of the quantum dot is plotted as a function of the temperature. We show the three phases of the dot in Fig. 4a. Note that the $\nu = 6$ phase exists as an excited configuration when the most probable Hartree–Fock solution is the $\nu = 5$ phase. Similarly, the $\nu = 4$ configuration exists as a possible excited configuration of the system even at fairly low temperatures. The specific heat, $C_v = d\langle H\rangle/dT$ (with T in units of eV), is shown in Fig. 4b. Clearly, when the energy undergoes a phase transition, the specific heat shows a sharp structure. This occurs since the energy is piece-wise continuous along the three phases. These calculations suggest that the quantum dot exhibits a band structure of many-body levels. The low-temperature states all have the same intrinsic shape characteristic (the same vortex structure). As we increase the temperature, other ν phases become accessible. At the point when two bands of different intrinsic character cross in energy, we find a phase transition. Similar phenomena are found in nuclear physics, where at higher nuclear excitation energies the eigenstates of the system may be of a different intrinsic deformation when compared to states of the ground-state band [21].

The occupation probabilities of the Fock–Darwin states, n_{FD}, for the temperature conditions of Fig. 3 are shown in Fig. 4c. In the low-temperature phase (3.9 K, solid line), the $l = 0$ state is occupied, while an edge reconstruction has occurred for the remaining five electrons. As we increase the temperature to 12 K (dotted line), we see a spreading

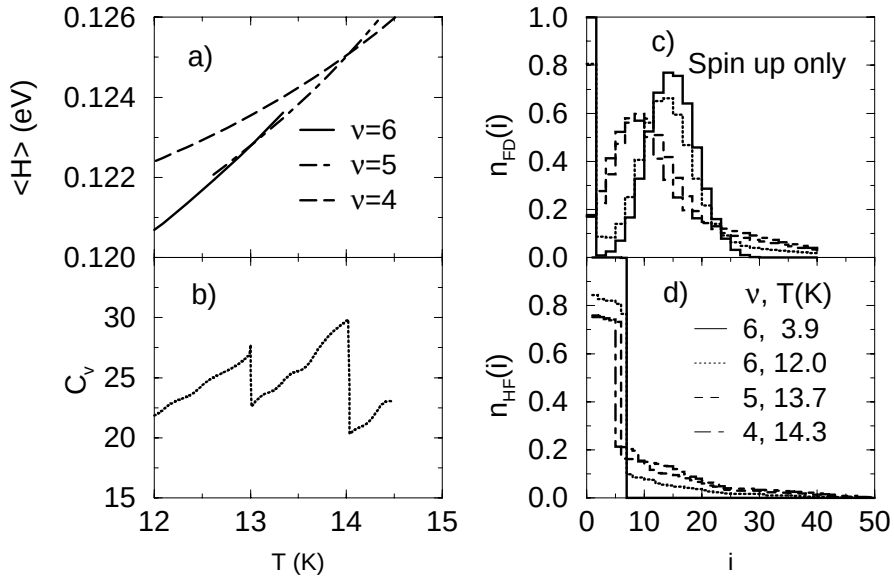

Figure 4. a) Expectation value of the energy as a function of temperature showing the three phases as discussed in the text. b) The specific heat for the lowest-energy configuration of the quantum dot as a function of temperature. c) Occupation of the Fock–Darwin states. d) Occupation of the Hartree–Fock states.

of the occupations in both the low and high angular momentum channels with about 0.8 particles in the $l = 0$ state. The $\nu = 5$ phase brings a dramatic decrease of occupation in the $l = 0$ state and a shift to lower angular momentum for the reconstructed edge. This trend continues after the $\nu = 4$ transition.

Signatures of the density transitions that we have seen also appear in the Hartree–Fock occupations n_{HF} as shown in Fig. 4d. At low temperatures (3.9 K) the familiar step-function behavior is evident from the figure. At 12 K in the $\nu = 6$ phase, we see a decrease of occupation to roughly 0.8 in the lowest six Hartree–Fock levels and a spreading to higher energy states. As the system undergoes the transition to $\nu = 5$, we see only five Hartree–Fock levels significantly filled (with $n_{HF} > 0.7$), and finally in the $\nu = 4$ phase, only four Hartree–Fock levels are significantly filled. The occupation number-spreading, which is due to thermal excitation of the system, is enhanced significantly when the system undergoes a phase transition.

The phase transitions that we have shown in the preceding discussion have definite observable consequences. In Fig. 5a we plot the chemical potential, that is, the separation energy $\Delta(N,T) = E_N(T) - E_{N-1}(T)$ to remove a particle from the quantum dot at a given temperature. Since this is an energy difference, $\Delta(N,T)$ will be influenced by transitions within both the $N = 6$ and $N = 5$ systems, and we expect changes in slope at the transition points. The $\nu = 5$ to $\nu = 4$ transition in the $N = 5$ dot occurs at roughly 12 K, causing a sharp rise in $\Delta(N = 6)$. A slope change in $\Delta(N = 6)$ is seen at ≈ 13 K, where

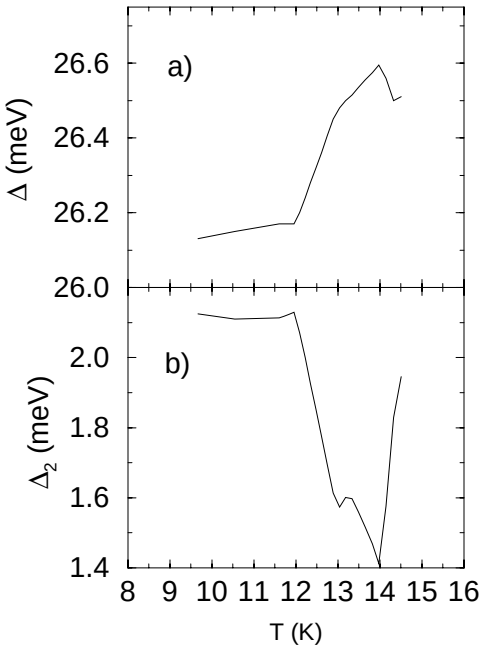

Figure 5. a) Chemical potential, Δ and b) inverse compressibility, Δ_2 for the $N = 6$ system as a function of the temperature.

the $\nu = 6$ to $\nu = 5$ transition occurs in the $N = 6$ system. The decrease from $14 - 14.3$ K occurs when the $N = 6$ system makes the transition from $\nu = 5$ to $\nu = 4$. A final change in slope occurs when the $N = 5$ dot makes the transition from $\nu = 4$ to $\nu = 3$. For the brief temperature interval when the $N = 6$ and $N = 5$ dots are in the same ν phase, we see a decrease in the chemical potential.

We observe similar changes in the inverse compressibility, $\Delta_2(N, T) = E_{N+1}(T) - 2E_N(T) + E_{N-1}(T)$. This quantity has been measured for quantum dots in low magnetic fields [22] and studied in Hartree–Fock theory for ground-state properties [23]. In our case, the $N = 7, 6$, and 5 dots participate in the observable. We again notice strong effects as one passes through transition points in either of the three systems contributing to the observable. Figure 5b shows $\Delta_2(N = 6)$ as a function of temperature. Before transitions occur, Δ_2 remains fairly constant. A large decrease begins at 12 K, where the $N = 5$ system undergoes its first transition. Interestingly, Δ_2 increases significantly when the $N = 6$ and $N = 5$ dots are in the $\nu = 4$ phase.

In addition to measurements of energy differences, one should be able to experimentally probe the thermal phase transitions using far-infrared spectroscopy and X-ray scattering. Far-infrared spectroscopy was used to investigate the excitations of InAs quantum dots as a function of the electron number per dot [24]. Grazing incidence X-ray scattering was recently used to generate a full structural characterization of quantum dots [25], including information on the elastic form factor. While these experiments were carried out at very low temperatures, it is conceivable that one could study the thermal response of quantum dots using X-ray or far-infrared scattering. A Fourier transform of the charge density

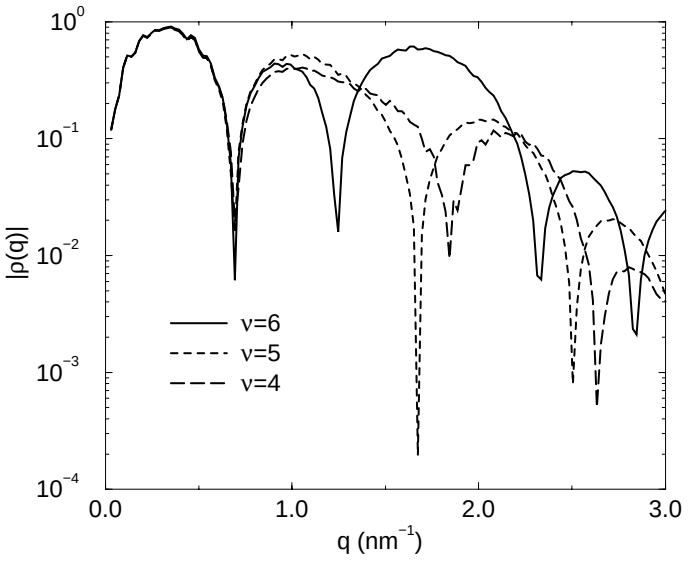

Figure 6. The form factor of the N=6 quantum dot is shown at different temperatures.

produced in our calculations gives the elastic form factor that can be used to characterize the dot.

We show in Fig. 6 the form factor, $\mid \rho(q) \mid$, as a function of the momentum transfer vector $\mid q \mid = \sqrt{q_x^2 + q_y^2}$. A well-defined minimum is apparent at approximately $\mid q \mid = 0.7\text{ev}^{-1}$ in all three phases. This first minimum is related to the size of the dot and clearly does not change in the three phases. This is apparent also from a close inspection of Fig. 3: while the internal structure changes significantly as a function of increasing temperature, the dot size does not change. The height of the second maximum slightly increases as in phase $\nu = 5$ before decreasing in the $\nu = 4$ phase. The position of the second minimum increases as a function of q significantly and would be a distinguishing feature in X-ray or far-infrared scattering experiments used to probe the thermal phases of a quantum dot.

3.2. A first application of AFMC techniques to the quantum dot

As the examples indicated above, the SMMC method, the nuclear implementation of the more general auxiliary field Monte Carlo (AFMC) technique, has been rather successful in describing various nuclear features. In this subsection, I will describe the AFMC technique as applied to calculations for quantum dots.

To calculate expectation values in AFMC, one makes use of the Euclidian-time many-body propagator $\hat{U} = \exp(-\beta \hat{H}$, where $\beta \equiv T^{-1}$ is interpreted as the inverse of the temperature. For example, the expectation value of some observable $\hat{\Omega}$ in a canonical ensemble, i.e., an ensemble with particle number N, can be obtained by calculating

$$\langle \hat{\Omega} \rangle = \frac{\mathrm{Tr}[\hat{P}_N \hat{U} \hat{\Omega}]}{\mathrm{Tr}[\hat{P}_N \hat{U}]} = \frac{\mathrm{Tr}_N[\hat{U}\hat{\Omega}]}{\mathrm{Tr}_N[\hat{U}]} \,, \tag{2}$$

where the many-body trace is defined as $\mathrm{Tr}\hat{X} \equiv \sum_i \langle i|\hat{X}|i\rangle$ and the sum is over all many-body states of the system. If $\hat{N}$ is the number operator, and $\hat{P}_N = \delta(N - \hat{N})$ is the

projector onto states with N electrons, the canonical ensemble is defined by $\mathrm{Tr}_N \hat{X} \equiv \sum_i \langle i|\hat{P}_N \hat{X}|i\rangle$. It is important to note that we cannot usually obtain detailed spectroscopic information (i.e., energies and wave functions) from AFMC. Rather, we can calculate expectation values of operators in the thermodynamic ensembles or the ground states [26].

In the AFMC method, two-body interactions in $\hat{H}$ are linearized through the Hubbard-Stratonovich (HS) transformation [27]. The difficult many-body evolution U is replaced by a superposition of an infinity of tractable one-body evolutions, each in a different fluctuating external field, σ. Integration over the external fields thus reduces the many-body problem to quadrature, which is evaluated stochastically.

With some rearrangement, the many-body Hamiltonian, $\hat{H}$, may be written schematically as

$$\hat{H} = \varepsilon\hat{\mathcal{O}} + \frac{1}{2}V\hat{\mathcal{O}}\hat{\mathcal{O}} \ , \tag{3}$$

where $\hat{\mathcal{O}}$ is a density operator of the form $a^\dagger a$, V is the strength of the two-body interaction, and ε a single-particle energy. In the full problem, there are many such quantities with various orbital indices that are summed over, but we omit them here for the sake of clarity.

All of the difficulty arises from the two-body interaction, that term in $\hat{H}$ quadratic in $\hat{\mathcal{O}}$. If $\hat{H}$ were solely linear in $\hat{\mathcal{O}}$, we would have a one-body quantum system, which is readily dealt with. To linearize the evolution, we employ the Gaussian identity

$$\begin{aligned} e^{-\beta\hat{H}} &= \sqrt{\frac{\beta \mid V \mid}{2\pi}} \int_{-\infty}^{\infty} d\sigma e^{-\frac{1}{2}\beta|V|\sigma^2} e^{-\beta\hat{h}} \ ; \\ \hat{h} &= \varepsilon\hat{\mathcal{O}} + sV\sigma\hat{\mathcal{O}} \ . \end{aligned} \tag{4}$$

Here, $\hat{h}$ is a one-body operator associated with a c-number field σ, and the many-body evolution is obtained by integrating the one-body evolution $\hat{U}_\sigma \equiv e^{-\beta\hat{h}}$ over all σ with a Gaussian weight. The phase, s, is 1 if $V < 0$ or i if $V > 0$. Equation (4) is easily verified by completing the square in the exponent of the integrand and then doing the integral.

With an expression of the form (4), it is straightforward to write observables as the ratio of two integrals. For example, the canonical expectation value (2) becomes

$$\langle\hat{\Omega}\rangle_N = \frac{\int d\sigma e^{-\frac{\beta}{2}|V|\sigma^2} \mathrm{Tr}_N \hat{U}_\sigma \hat{\Omega}}{\int d\sigma e^{-\frac{\beta}{2}|V|\sigma^2} \mathrm{Tr}_N \hat{U}_\sigma} \ , \tag{5}$$

which can be more conveniently written as

$$\langle\hat{\Omega}\rangle_N = \frac{\int d\sigma W_\sigma \Omega_\sigma}{\int d\sigma W_\sigma} \ ; \tag{6}$$

where $W_\sigma = G_\sigma \mathrm{Tr}_N \hat{U}_\sigma$, $G_\sigma = e^{-\frac{\beta}{2}|V|\sigma^2}$ and $\Omega_\sigma = (\mathrm{Tr}_N \hat{U}_\sigma\hat{\Omega})/(\mathrm{Tr}_N \hat{U}_\sigma)$. Thus, the many-body observable is the weighted average (weight W_σ) of the observable Ω_σ calculated in a canonical ensemble involving only the one-body evolution $\hat{U}_\sigma$. Similar expressions involving two σ fields (one each for $e^{-\tau\hat{H}}$ and $e^{-(\beta-\tau)\hat{H}}$) can be written down for the response function.

An expression of the form (6) has a number of attractive features. First, the problem has been reduced to quadrature—we need only calculate the ratio of two integrals. Second, all of the quantum mechanics (which appears in Ω_σ) is of the one-body variety, which scales simply with the square of the number of single-particle states included in the calculation. The price to pay is treating the one-body problem for all possible σ fields.

Since $\hat{H}$ contains many two-body terms that do not commute, the evolution must be discretized via the Trotter approximation, i.e., $\beta = N_t \Delta\beta$, before applying the HS transformation, i.e.,

$$Z_N = \mathrm{Tr}_N e^{-\beta \hat{H}_{ee}} \rightarrow \mathrm{Tr}_N \left[e^{-\Delta\beta \hat{H}_{ee}} \right]^{N_t} \rightarrow \int \mathcal{D}[\sigma] G(\sigma) \mathrm{Tr}_N \prod_{n=1}^{N_t} e^{\Delta\beta \hat{h}(\sigma_n)} \ , \tag{7}$$

where σ_n are the auxiliary fields at a given imaginary time-step $\Delta\beta$ (there is one σ-field for each two-body matrix-element in $\hat{H}_{ee}$ when the two-body terms are recast in quadratic form), $\mathcal{D}[\sigma]$ is the measure of the integrand, $G(\sigma)$ is a Gaussian in σ, and $\hat{h}$ is a one-body Hamiltonian. Thus, the many-body problem is transformed from the diagonalization of a large matrix to one of large dimensional quadrature. Dimensions of the integral can reach up to 10^5 for systems of interest, and it is thus natural to use Metropolis random walk methods to sample the space. The accuracy of its results are limited only by sampling and discretization errors which may be controlled. Because the numerical effort for AFMC scales only as a low power of the problem size, very large (and hence more realistic) calculations are possible. Further, because the calculations are compute-intensive, with relatively modest memory or I/O, they are ideally suited to take advantage of developments in parallel high-performance computing.

The most significant challenge to applying the AFMC method resides in overcoming the fermion-sign problem. The fermion-sign problem manifests itself in more than a single way (e.g., Monte Carlo integration errors, numerical instabilities, etc.). Algorithmic solutions to these problems are typically not robust and are highly dependent on the fermion system to which they are applied. For example, systems whose interactions are purely attractive are free of the sign problem [26]. In application to the nuclear shell model, where dominant components of the force are attractive, practical solutions to the sign problem are based on an extrapolation of observables calculated from nearby families of Hamiltonians which do not exhibit the sign problem. Success, in this case, depends crucially on the degree of extrapolation required.

For our system of many-electrons confined in a quantum dot, the Coulomb forces are purely repulsive. (If the system is represented in a basis in which the two-body interactions are diagonal, then the effective forces have both attractive and repulsive character.) In computing expectation values of observables as in Eq. (2), we will employ the finite-temperature methods discussed above. At high temperatures, these methods will not suffer from a Monte Carlo sign problem, but at lower temperatures, we will encounter the infamous sign problem. Its most frequent manifestation occurs when the weight functions used for a Metropolis Monte Carlo evaluation of the integrals introduced by the Hubbard-Stratonovich transformation lose their positive-definite character [26].

As a first example of an AFMC application to quantum dots, I show in Fig. 7 results for the $N = 6$ system as a function of inverse temperature. The energy of the system decreases as a function of inverse temperature, as it should, and the Monte Carlo sign

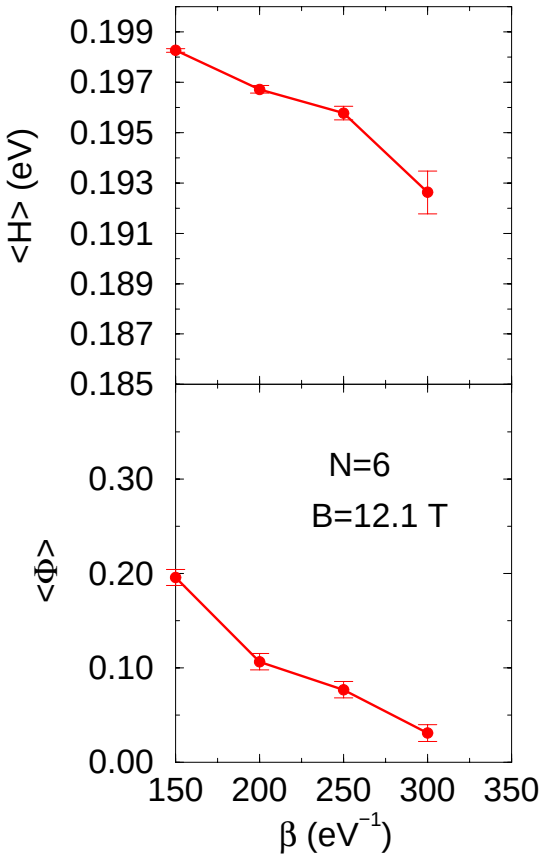

Figure 7. Top: expectation of the energy as a function of inverse temperature. Bottom: the Monte Carlo sign for this system.

shows the typical behavior of becoming small very quickly. We are exploring methods to stabilize the AFMC against the sign problem when the effective interactions include terms that are both attractive and repulsive [28,29].

4. Conclusion

Confined quantum-mechanical systems exhibit a variety of interesting phenomena. Nuclear shapes range from spherical (near closed shells) to well deformed (in mid-shell systems), to those shapes with special symmetries such as the γ-soft nuclei in the ^{124}Xe region. Quantum dots also show interesting shape changes as one adds electrons at a given magnetic-field strength and temperature. The shells that are built up in quantum dots at high magnetic fields are somewhat different in character from those found in nuclei. For example, in the oscillator basis the doubly magic nucleus, ^{40}Ca, can be considered as a core, and hence inert, system in calculations of low-lying states in the mid-fp shell. In contrast to this behavior, the oscillator levels are all active at high magnetic fields.

Nuclei can change their character as a function of cranking frequency. The signature for such a change is a level crossing in J_z as a function of the cranking frequency. Furthermore, the same nucleus can have different bands built upon different intrinsic structures within the same nucleus. This is also true in quantum dots. I indicated how a dot

goes through phase transitions as a function of temperature and how different intrinsic structures are evident during the transitions. The thermal phase transitions should be experimentally verifiable by investigating fluctuations of the chemical potential as a function of temperature and with far-infrared scattering.

Finally, I briefly discussed the ingredients needed to pursue AFMC calculations for quantum dots. Development of the AFMC method for applications in quantum dots continues and should prove to be an excellent area in which to apply techniques developed in nuclear physics to other areas of science.

REFERENCES

1. D. Rudolph, *et al.*, Phys. Rev. Lett. **82** (1999) 3763.
2. T. Mizusaki, *et al.*, Phys. Rev. **C59** (1999) R1846.
3. Y. Alhassid, *et al.*, Phys. Rev. Lett. **77** (1996) 1444.
4. D.J. Dean, *et al.*, Phys. Lett. **B317** (1993) 275.
5. J.A. White, *et al.*, Phys. Rev. **C61** (2000) 044327.
6. T. Motobayashi *et al.*, Phys. Lett. **B346** (1995) 9.
7. D.J. Dean, *et al.*, Phys. Rev. **C59** (1999) 2474.
8. P.-G. Reinhard, *et al.*, Phys. Rev. **C60** (1999) 014316.
9. X. Campi, *et al.*, Nucl. Phys. **A251** (1975) 193.
10. M. Hjorth-Jensen, *et al.*, Phys. Rep. **261** (1995) 125.
11. A. Abzouzi, *et al.*, Phys. Rev. Lett. **66** (1991) 1134.
12. B. Barmore, *et al.*, in preparation.
13. E.K. Warburton, *et al.*, Phys. Rev. **C41** (1990) 1147.
14. T.H. Oosterkamp, *et al.*, Phys. Rev. Lett. **82** (1999) 2931.
15. R. C. Ashoori, Nature **379** (1996) 413.
16. C. Chamon, *et al.*, Phys. Rev. B **49** (1994) 8227.
17. H.-M. Müller and S.E. Koonin, Phys. Rev. B **54** (1996) 14532.
18. S.M. Reimann, *et al.*, Phys. Rev. Lett. **83** (1999) 3270.
19. L. Jacak, P. Hawrylak, and A. Wójs, *Quantum Dots*, (Springer, Berlin, 1997).
20. D.J. Dean, *et al.*, submitted to Phys. Rev. Lett. (2000).
21. D.G. Sarantites, *et al.*, Phys. Rev. **C57** (1998) R1.
22. U. Sivan *et al.*, Phys. Rev. Lett. **77** (1996) 1123; S.R. Patel *et al.*, Phys. Rev. Lett. **80** (1998) 4522.
23. S. Levit, D. Orgad, Phys. Rev. **B60** (1999) 5549.
24. M. Fricke *et al.*, Europhys. Lett. **36** (1996) 197.
25. T.H. Metzger, *et al.*, Thin Solid Films **336** (1998) 1.
26. S.E. Koonin, *et al.*, Phys. Repts. **278** (1997), 1.
27. J. Hubbard, Phys. Rev. Lett. **3** (1959) 77; R.L. Stratonovich, Dokl. Akad. Nauk. S.S.S.R. **115** (1957) 1097.
28. R. Baer Chem. Phys. **109** (1998) 6219.
29. S. Zhang et al Phys. Rev. **B55** (1997) 7464.